coatings

MDPI

Article

Flexible Piezoelectric 0–3 PZT@C/PDMS Composite Films for Pressure Sensor and Limb Motion Monitoring

Chungang Li [1], Chao Li [2], Yingzi Wang [3], Yaoting Zhao [1], Fengzhen Yang [1], Gensheng Dong [1], Xiujuan Lin [1], Shifeng Huang [1] and Changhong Yang [1,*]

[1] Shandong Provincial Key Laboratory of Preparation and Measurement of Building Materials, University of Jinan, Jinan 250022, China
[2] Shandong Institute for Product Quality Inspection, Jinan 250100, China
[3] School of Materials Science and Engineering, University of Jinan, Jinan 250022, China
* Correspondence: mse_yangch@ujn.edu.cn

Abstract: The flexible piezoelectric pressure sensor is essential in areas such as machine sensing and human activity monitoring. Here, 0-dimensional PZT piezoelectric ceramic nanoparticles with carbon coating were synthesized by a surface-modified technique. The excellent electrical conductivity of the carbon shell causes redistribution and accumulation of mobile charges in the carbon layer, resulting in a greatly increased piezoelectric effect by inducing an enhanced electric field. A series of organic–inorganic composite films were prepared by the spin-coating method using polydimethylsiloxane (PDMS) as the matrix. The as-fabricated flexible PZT@C/PDMS composite film with 40 wt% PZT@C powder exhibits an excellent output voltage of ~74 V, a peak of output current ~295 nA, as well as a big sensitivity of 5.26 V N^{-1}. Moreover, the composite film can be used as a pressure sensor to detect changes in force as well as for monitoring limb movements such as finger flexion, wrist flexion, and pedaling. This study reveals the promising applications of flexible 40%PZT@C/PDMS composite film for limb motion monitoring and pressure sensing.

Keywords: flexible; piezoelectric; surface modification; composite material; sensor; monitoring

check for updates

Citation: Li, C.; Li, C.; Wang, Y.; Zhao, Y.; Yang, F.; Dong, G.; Lin, X.; Huang, S.; Yang, C. Flexible Piezoelectric 0–3 PZT@C/PDMS Composite Films for Pressure Sensor and Limb Motion Monitoring. *Coatings* **2024**, *14*, 1269. https://doi.org/10.3390/coatings14101269

Academic Editor: Denis Nazarov

Received: 6 September 2024
Revised: 26 September 2024
Accepted: 29 September 2024
Published: 3 October 2024

Copyright: © 2024 by the authors. Licensee MDPI, Basel, Switzerland. This article is an open access article distributed under the terms and conditions of the Creative Commons Attribution (CC BY) license (https://creativecommons.org/licenses/by/4.0/).

1. Introduction

In contemporary society, the advancements of Internet of Things (IoT) and Artificial Intelligence (AI) technologies increased demand for smart wearable devices that can sense, monitor, and record human physiological parameters [1–4]. The pressure sensors, as a type of sensor, play a vital role in external pressure monitoring and sensing human limb activity because of their sensitivity and versatility [5,6]. According to the different sensing mechanisms, the pressure sensors can be grouped into three types: piezoelectric [7–9], capacitive [10,11], and piezoresistive sensors [12–14]. Among them, the piezoelectric sensor has the advantages of high sensitivity and good dynamic response and became a popular choice for detecting dynamic pressure and human limb activity [15].

Piezoelectric materials, as functional materials, can be deformed to generate polarized charge when excited by external mechanical stress, e.g., human body limb movement. Within the material, a piezoelectric potential can be formed, thus realizing the conversion of mechanical energy to electrical energy [16]. Currently, conventional piezoelectric sensors widely use inorganic piezoelectric materials such as Pb(Zr, Ti)O_3 (PZT) [17], $BaTiO_3$ [18], (K, Na)NbO_3 (KNN) [19], $PbTiO_3$ [20], and ZnO [21], etc., as piezoelectric functional phases. In particular, it is noteworthy that PZT piezoelectric ceramics are widely used owing to their outstanding piezoelectric properties, such as high piezoelectric coefficients (d_{33}) [22]. However, the inherent properties, such as high stiffness, brittleness, and limited deformation, make them unsuitable for use in flexible electronics, such as wearable devices and sensing applications with curved structures [23]. The polymer materials, such as polyvinylidene difluoride (PVDF), polydimethylsiloxane (PDMS), and polyimide (PI), are more flexible

but have lower piezoelectric properties compared to piezoelectric ceramics. Hence, organic-inorganic material composites are successful in combining the high piezoelectric properties of piezoelectric ceramics with the flexibility advantages of polymer materials.

At present, the main focus of research is on enhancing the properties of composites through the incorporation of various piezoelectric fillers, including one-dimensional (1D) nanowire/fiber, two-dimensional (2D) monolithic/sheet, three-dimensional (3D) piezoelectric ceramic skeleton, and zero-dimensional (0D) nanoparticles (NPs). For example, Md. Jahirul Islam et al. [24] prepared a PVDF-ZnO composite film with the spin coating method by doping ZnO particles into the PVDF matrix, and the open circuit voltage of the composite film was increased to 4.2 V compared with pure PVDF film. Seong Su Ham et al. [25] developed a flexible sensor possessing an open-circuit voltage of ~5 V by doping KNN 0D piezoelectric particles into the poly(vinylidene fluoride-trifluoroethylene) [P(VDF-TrFE)]. Mukesh Kumar et al. [26] prepared BT/PVDF 2D composite films by electrospinning with a peak voltage of 8.22 V and a short circuit current of 3.36 μA.

Nevertheless, with the addition of these piezoelectric phases, the piezoelectric properties of the composites tend to show a trend of increasing and then decreasing. The primary cause is that with the significant increase in fillers, the aggregation trend between particles is obviously enhanced, resulting in the destruction of the continuity of the polymer matrix and the reduction in the piezoelectric potential.

In this work, PZT@C piezoelectric ceramic NPs with different carbon shell thicknesses were obtained by polydopamine (PDA) modification and high-temperature carbonization, based on PZT ceramic NPs synthesized by conventional solid-phase method. A series of PZT@C/PDMS composite films were prepared via the spin-coating technique, and the PZT/PDMS composite films were studied for comparison. The morphology structure and electrical properties were characterized. The as-fabricated flexible PZT@C/PDMS composite films with 40 wt% PZT@C powders have a large output voltage of ~74 V, a merit output current of ~295 nA, as well as a high sensitivity of 5.26 V N^{-1}. In addition, the 40% PZT@C/PDMS composite film can be used as the core functional layer of a pressure sensor to monitor body motions and concrete structure pressure.

2. Materials and Methods

2.1. Fabrication of PZT Nanoparticles

The PZT ceramics were prepared using conventional solid-phase sintering methods (see Figure S1). The PZT powder used in this work is a commercial half-product of PZT (Yu Hai Electronic Ceramics Co., Ltd., Zibo, China). Firstly, a certain quantity of PZT ceramic powder was thoroughly mixed with ethanol by ball milling for 12 h. Then, the ceramic powder was dried in a high-temperature oven at 80 °C for 5 h. After that, it was calcined in an alumina crucible at 800 °C for 2 h. The ceramic particles were sieved through a 60-mesh sieve, added with a polyvinyl alcohol (PVA) binder, and pressed into pellets ($\Phi 10 \times 1$ mm^3) at a pressure of 6–8 MPa for 1 min. Next, the ceramic pellets were embedded in an alumina crucible sintered at 1160–1170 °C for 2 h and cooled to room temperature at 5 °C/min for crystallization. Finally, the sintered ceramic pellets were crushed in an agate mortar and ball-milled for 8 h. The ceramic powder was dried at 80 °C for 5 h and passed through 100-mesh and 300-mesh sieves to obtain PZT NPs.

In addition, for electrical performance testing, the ceramic samples were polished, cleaned, silver-plated with electrodes, and sintered with conductive silver paste at 560 °C for 30 min. Finally, the PZT ceramic pellets were placed in silicone oil at 110 °C and polarized under a 40 kV/cm electric field for 20–30 min, followed by piezoelectric performance testing.

2.2. Preparation of Carbon Coated PZT Piezoceramic Particles and Composite Films

PZT piezoceramic particles prepared were taken as raw materials. Firstly, the precursor PZT@PDA particles were prepared through surface modification of PZT ceramic particles with dopamine hydrochloride (PDA) (Macklin Biochemical Technology Co., Ltd., Shanghai, China). PZT NPs were dispersed into an aqueous PDA solution (Tris-HCl solution, 10 mM,

pH = 8.5) with continuous stirring for 24 h. As a note, the correlation between the weight ratio of PZT and PDA would affect the thickness of the carbon shell encapsulated by the ceramic particles. In this work, the carbon shell thickness (~7 nm, ~13 nm, ~16 nm, and 40–60 nm) of ceramic particles was investigated for different mass ratios (8:1, 6:1, 4:1, and 2:1) of PZT and PDA. Upon completion of the reaction, the mixed suspension was placed in a centrifuge (H1850, Huan Xiangyi Laboratory Instrument Development Co., Ltd., Hunan, China) and filtered at 8000 rpm for 15 min to obtain the precipitation of PZT@PDA. Then, the as-fabricated PZT@PDA particles were washed at least five times with deionized water to completely remove residual chloride ions and dried continuously in an oven at 80 °C for 12 h. Subsequently, the PZT@PDA powder was heated to 550 °C and held under the argon protection for 2 h to prepare the carbon shell structure.

Finally, the PDMS (Sylgard 184, Dow Inc., Midland, MI, USA) resin was prepared using a mass ratio of 10:1 for the base elastomer and curing agent. Weight 2 g of base elastomer and 0.2 g of curing agent into a beaker, and then magnetically stirred for 15 min. The PZT@C powder with various weight fractions of 5, 10, 20, 30, and 40 wt% were uniformly dispersed into the PDMS matrix. The well-mixed and consistent precursor was obtained by stirring for 3 h and sonicating for 15 min, successively. Then, the precursor was placed in a vacuum desiccator for 15 min to remove the gases in the solution, followed by injecting into a prepared glass mold and spin-coating at 500 rpm for 15 s to form a film ($20 \times 30 \times 1$ mm^3). Then the film was put into a vacuum drying oven to cure for 4 h under the condition of 80 °C negative pressure of 0.8 MPa. To assemble into a device, two Cu foils were fixed on the surface of composites as electrodes. The PZT@C/PDMS composites were polarized at 60 °C for 24 h in a direct current field of 80 kV/cm. The preparation process of PZT@C/PDMS composite films is schematically shown in Figure 1.

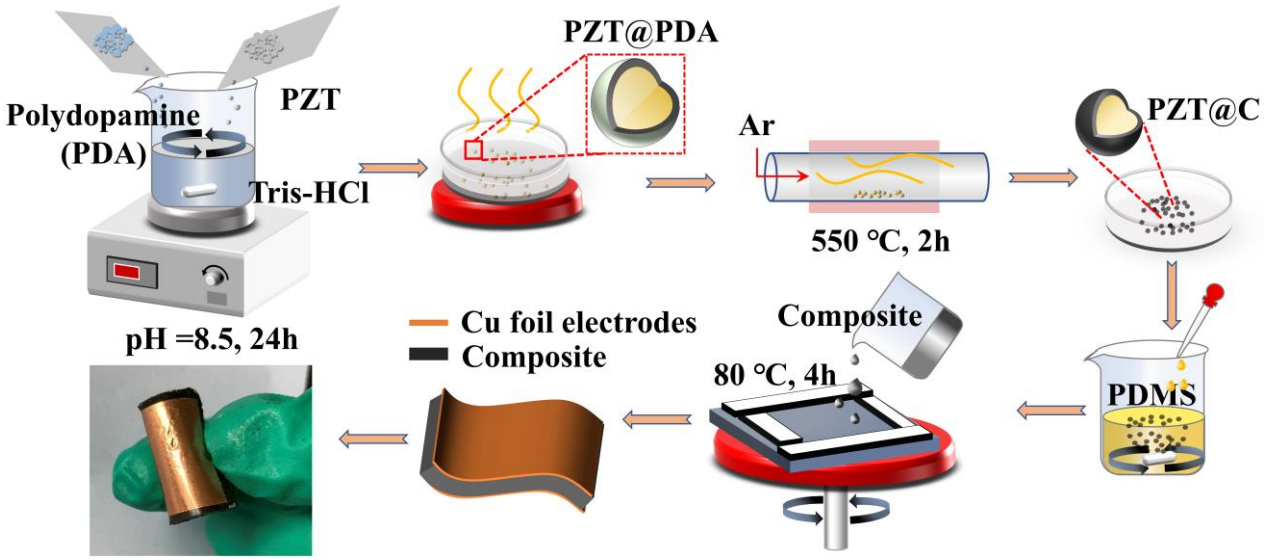


Figure 1. Schematic process diagram of the fabrication process for PZT@C/PDMS composite films.

2.3. Material and Device Characterization

The dielectric constant (ε_r) and dielectric loss (tan δ) were characterized by an impedance analyzer (HP4294A, Agilent, Santa Clara, CA, USA). The ferroelectric polarization hysteresis (*P-E*) loops and current density-electric field (*J-E*) curves were obtained using a ferroelectric testing system (aixACCT, Aachen, Germany). The d_{33} was obtained by the quasi-static tester (ZJ-6A, Institute of Acoustics, Beijing, China). Morphology and element mapping of the ceramic powder were observed by scanning electron microscopy (SEM, GeminiSEM360, Carl Zeiss AG, Jena, Germany). The range of ceramic particles size distribution was obtained by testing with a laser particle size analyzer (2000, Mastersizer, Worcestershire, UK). A transmission electron microscopy (TEM) image was obtained using an electron

microscope (JEM-2100F, JEOL Ltd., Tokyo, Japan). The phase structure analysis was tested by X-ray diffraction in the range of 2θ from 20° to 60° (XRD, D8 ADVANCE, Karlsruhe, Germany). The Raman spectrum (HR Evolution, Horiba, Chiyoda, Japan) was used to acquire the crystal structure of the carbon shell. The viscosities of the precursor were experimentally determined by a rheometer (Kinexus Lab+, Netzsch, Germany) at various shear rates. The stress–strain curves were acquired using an electronic universal material testing machine (5669, INSTRON, Norwood, MA, USA). An oscilloscope (MDO34, Tektronix, Beaverton, OR, USA) was used to capture the output voltage of the device. The output current was captured by a digital source meter (2450, Keithley, Cleveland, OH, USA).

3. Results and Discussion

3.1. Electrical Properties of PZT Ceramic

Figure 2 demonstrates the basic electrical properties of PZT ceramics. The temperature-dependent ε_r and tan δ for PZT ceramic samples at 1 kHz are shown in Figure 2a. The ε_r and tan δ of the sample can be reached at 5961 and 1.2%, respectively. The peak of ε_r/tan δ of ~360 °C for the sample is observed within the temperature range, which corresponds to T_c and the ferroelectric paraelectric phase transition temperature. The d_{33} is on the order of 520 pC/N at room temperature (see Figure S2). Figure 2b exhibits the *P-E* loops of the ceramics measured at 1 Hz under the varied electric fields from 5 to 45 kV/cm at room temperature. Clearly, the ceramic sample exhibits typical *P-E* loops with a relatively rectangular shape. All *P-E* loops without the obvious conduction phenomenon are symmetrical, showing typical ferroelectric features. The remnant polarization (P_r) and the coercive field (E) can reach up to 22 μC/cm^2 and 12 kV/cm, respectively, with the applied electric field of 45 kV/cm. A typical *J-E* curve exhibits a normal ferroelectric feature, as seen in Figure 2c.

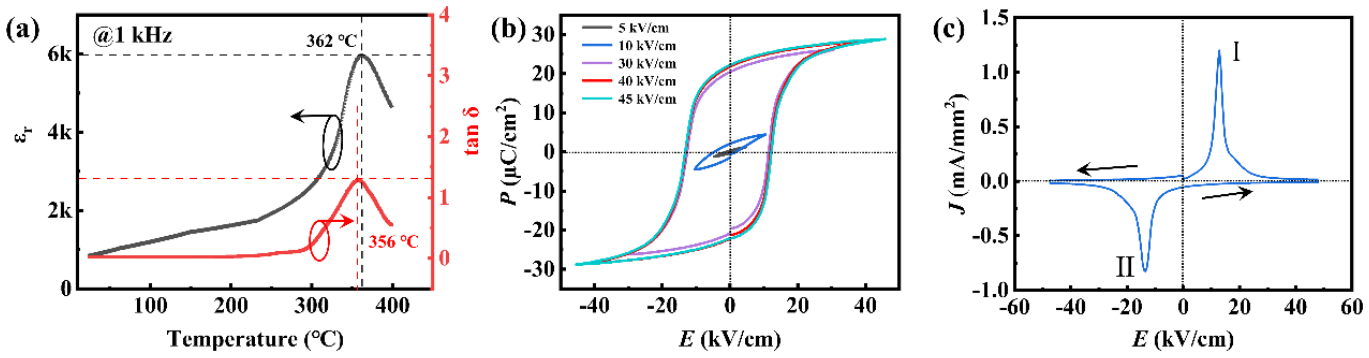


Figure 2. Electrical properties of PZT ceramics: (**a**) the variations in ε_r and tan δ with temperature, (**b**) *P-E* loops at various electric fields, and (**c**) *J-E* loop at 45 kV/cm electric field.

In the initial state, the domains are in a disordered randomly oriented state. When an electric field is applied to the ceramic, the randomly oriented domains are reordered along the direction of the electric field, resulting in a current density peak (peak I) in the first quadrant. Similarly, corresponding to a current peak (II) in the third quadrant, this is the result of applying an electric field in the opposite direction, and the domains will also follow the direction of the electric field to flip [27]. These results above fully prove that the PZT ceramics prepared in this work are in ferroelectric and dielectric states.

3.2. Performance of Piezoelectric Composite Films

Figure 3 shows the basic characterization of the composite film. The piezoelectric function phase of PZT has the features of polyhedral shape and relative homogeneity, as presented in Figure 3a. The illustration in Figure 3a shows that the diameter of piezoelectric ceramic particles is concentrated at ~270 nm. To check the chemical composition of the ceramic particles, the typical energy dispersive spectroscopy (EDS) is exhibited in Figure 3b,

where Pb, Zr, Ti, and O elements are distributed homogeneously. Figure 3c demonstrates the optical photographs of PZT and PZT@C ceramic NPs. Obviously, the macroscopic color of the ceramic powder changed from light yellow to pure black after being coated with carbon. Figure 3d displays the XRD patterns of PZT, PZT@C powders, and a series of composite films. All diffraction characteristic peaks of the composite films and PZT@C powder can be well matched with PZT ceramic, indicating that the crystal structure of PZT is not affected by the carbon shell or PDMS matrix. This may be due to the fact that the carbon shells are merely wrapped around the surface of the particles and do not change the phase structure of PZT.

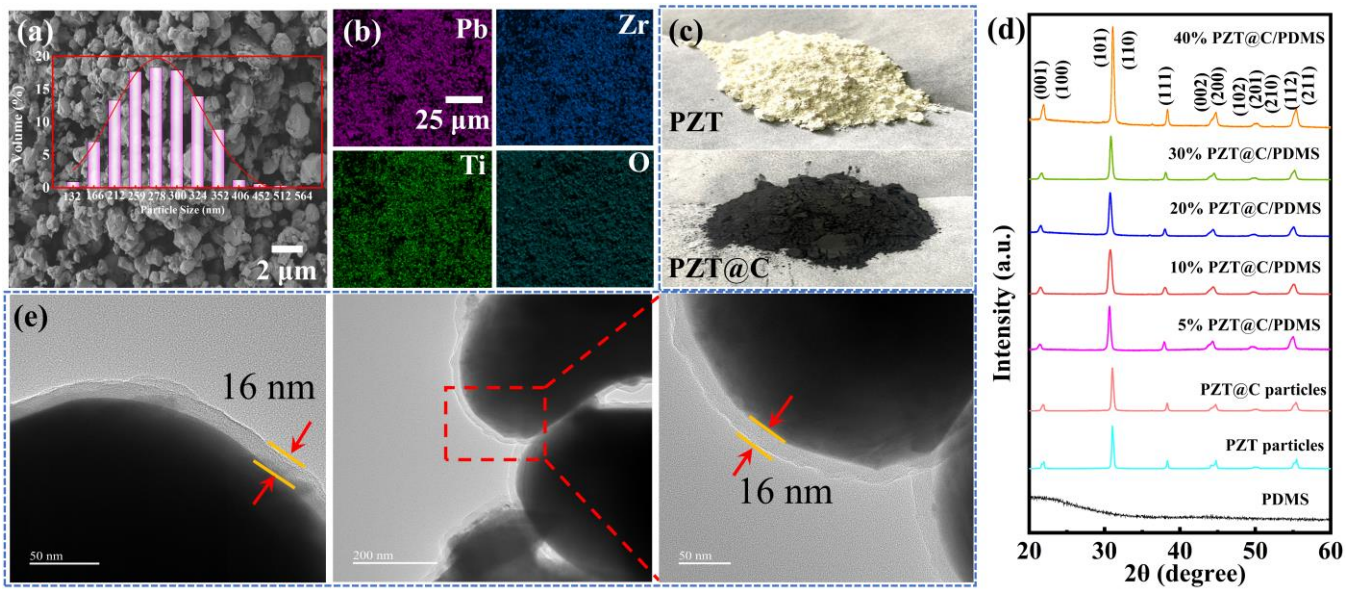


Figure 3. (**a**) SEM image of PZT ceramic power, the inset is diameter distribution of ceramic power. (**b**) EDS mappings. (**c**) The Optical pictures of PZT and PZT@C particles. (**d**) X-ray diffraction patterns of PDMS, PZT powder, PZT@C particles, and PZT@C/PDMS composite films. (**e**) TEM images of PZT@C particles.

The TEM images of the PZT@C powder (Figure 3e) show the carbon is well dispersed and uniformly adhered on the surface of the PZT powder, and the thickness of the carbon shell is ~16 nm. All TEM images of PZT@C powder with different PZT and PDA mass ratios are exhibited in Figure S3. Obviously, these results indicate that the thicknesses of carbon shells are ~7 nm, ~13 nm, ~16 nm, and 40–60 nm, respectively, when the mass ratios of PZT and PDA are 8:1, 6:1, 4:1, and 2:1. In the Raman spectra of PZT and PZT@C NPs shown in Figure S4, a D peak at 1357 cm^{-1} and a G peak at 1582 cm^{-1} can be observed, which corresponds to diamond-like carbon (sp^3 bonds) and graphite-like carbon (sp^2 bonds). This also demonstrates that the surface of PZT particles was coated by the typical amorphous carbon structure, which has good electrical conductivity [28,29]. Based on the previous reports [30], the mass ratio of PZT and PDA with a carbon shell of ~16 nm is chosen to be 4:1 for the composites prepared in this work. Figure S5a shows the cross-sectional SEM images of the 40%PZT/PDMS composite film. The agglomeration phenomenon of PZT particles is observed in the composite film due to the large disparity in elasticity modulus between stiff PZT particles and the soft PDMS matrix [31]. For the 40%PZT@C/PDMS composite film, it can be seen that the ceramic particles are uniformly dispersed, with no obvious particle agglomeration over a large area, as displayed in Figure S5b.

In terms of rheological properties, the shear stress versus shear rate is plotted as shown in Figure 4a. With the increase in the weight ratio for PZT@C ceramic powder, the shear stress shows an obvious upward trend. At the large shear rate of 400 s^{-1}, when the mass fraction of PZT@C is 0, 5%, 10%, 20%, 30%, and 40%, the corresponding shear

stress of the PZT@C/PDMS slurry reaches 1460 Pa, 1802 Pa, 1860 Pa, 1962 Pa, 2376 Pa, and 2666 Pa, respectively. Figure 4b shows the viscosity as a function of the shear rate for the PZT@C/PDMS composite materials with different PZT@C weight ratios from 0 to 40 wt%. As the solid loading of PZT@C continues to increase, the viscosity and the degree of shear-thinning behavior also increase significantly. For a varying solid loading range from 0 to 20 wt%, the PZT@C/PDMS composites show the slight shear-thinning behavior and marked shear plateau. The degree of shear-thinning behavior increases significantly as the solid loading rises to 30 and 40 wt% without a significant shear plateau. In addition, since the high viscosity of PZT@C/PDMS material would limit the fluidity of slurry, the highest mass ratio of PZT@C and PDMS is limited to 4:6 in this work in order to ensure that the film has both excellent mechanical and electrical properties.

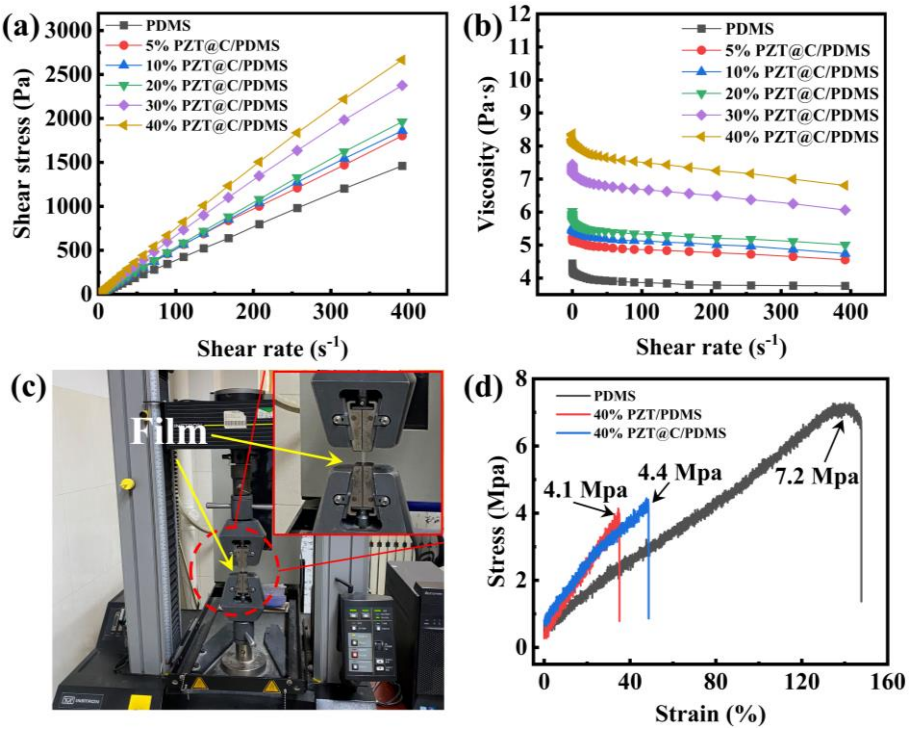


Figure 4. (**a**) The shear stress versus shear rate. (**b**) The viscosity versus shear rate. (**c**) Optical photo of the tensile test process. (**d**) Tensile stress–strain curves.

Figure 4c reveals the optical photo of the tensile test process. The tensile state of the composite films was carried out by an electronic universal testing machine, and the tensile rate was 0.5 mm/min. Figure 4d displays the representative stress-strain curves for composite films and the pure PDMS film. Specifically, the strain of the pure PDMS film reaches 147%, and the tensile properties of the composite film decrease significantly when the inorganic piezoelectric fillers are introduced. This may be because the introduction of the rigid inorganic ceramic phase leads to an increase in stiffness and a decrease in tensile properties. Meanwhile, the strain of the composite film prepared by modified ceramic particles (PZT@C) reaches 48%, which is better than 34% of the PZT/PDMS film. Obviously, the tensile property of the 40% PZT@C/PDMS composite film is higher than that of the 40% PZT/PDMS film. Usually, the macroscopic mechanical properties are directly related to the microstructure of the film. This enhancement can be attributed to the modified carbon shell on the surface of ceramic particles, facilitating better dispersion of PZT in the PDMS matrix.

Figure 5a presents the ε_r comparison diagram of the composite films at 1 kHz. It can be seen that the ε_r gradually increases with increasing the content of piezoelectric fillers. The dielectric constants of the composite films with PZT@C powder as the piezoelectric phase are obviously bigger than those of PZT ceramic material. Similarly, a

higher piezoelectric constant is also achieved by increasing the content of the piezoelectric phase, as demonstrated in Figure 5b. The piezoelectric d_{33} of the composite film increases from ~15 to ~41 pC/N with the increasing of PZT@C content from 5 to 40 wt%. The d_{33}~41 pC/N of 40% PZT@C/PDMS films was significantly enhanced compared to pure PDMS (d_{33}~7 pC/N) and 40% PZT/PDMS films (d_{33}~22 pC/N) after the same poling process. Compared with the pure PDMS (d_{33}~7 pC/N) and 40% PZT/PDMS film (d_{33}~22 pC/N), the d_{33} value increases to ~41 pC/N with a PZT@C content of 40 wt% under the same preparing process. Figure 5c displays the ferroelectric *P-E* loops of the PZT@C/PDMS composite films. It can be seen that the more PZT@C, the stronger the ferroelectric property.

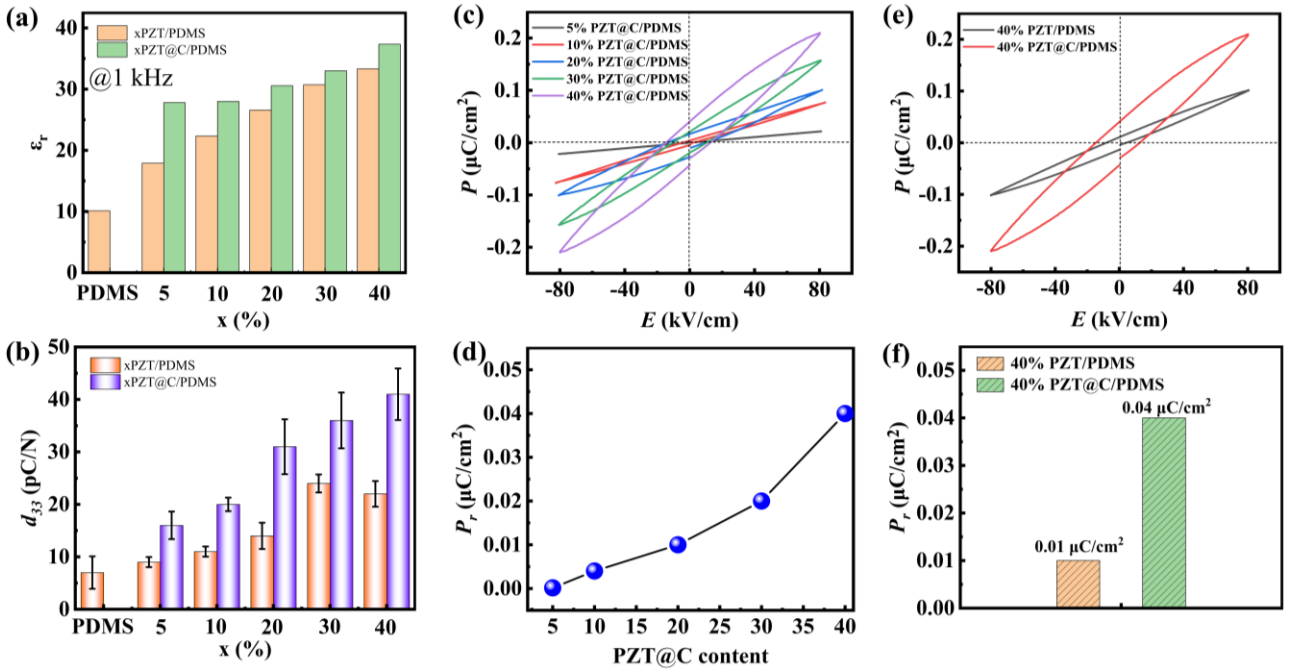


Figure 5. Comparisons of (**a**) dielectric constants and (**b**) piezoelectric coefficient. (**c**) *P-E* loops. (**d**) P_r for composite films with different contents of PZT@C. Comparisons of (**e**) *P-E* loops and (**f**) P_r.

As shown in Figure 5d, with the increase in piezoelectric filler content, the residual polarization of the composite film shows an upward trend. Figure 5e illustrates the *P-E* loops of the 40% PZT/PDMS and 40% PZT@C/PDMS composite films. Compared to the 40% PZT/PDMS composite film, the 40% PZT@C/PDMS composite film has better ferroelectric properties with a higher P_r (Figure 5f) under the same driving electric field.

The impact of various ceramic powder loadings on the electrical output of the composite films is investigated. Figure 6a,b shows the output voltage and current of the PZT/PDMS composite films under the excited condition of a human hand. The peak output voltage and current display an increasing and then decreasing trend as the piezoelectric filler content increases from 0 to 40%. The highest output signal of ~50 V is obtained when filled with 30 wt% PZT powder. The excessive addition of fillers leads to particle agglomeration, which reduces the interfacial specific surface area and destroys the microstructure of the film [20]. This result is also consistent with the trend of piezoelectric properties (d_{33}) of PZT/PDMS composite films (Figure 5b). The SEM images of the agglomeration phenomenon are demonstrated above (see Figure S5). In addition, pure PDMS flexible films were prepared in order to exclude the effect of triboelectricity on the electrical output. Under the condition of finger pressing, this film shows a very low electrical output signal of almost zero. The results suggest that the triboelectric effect is severely limited during the test process.

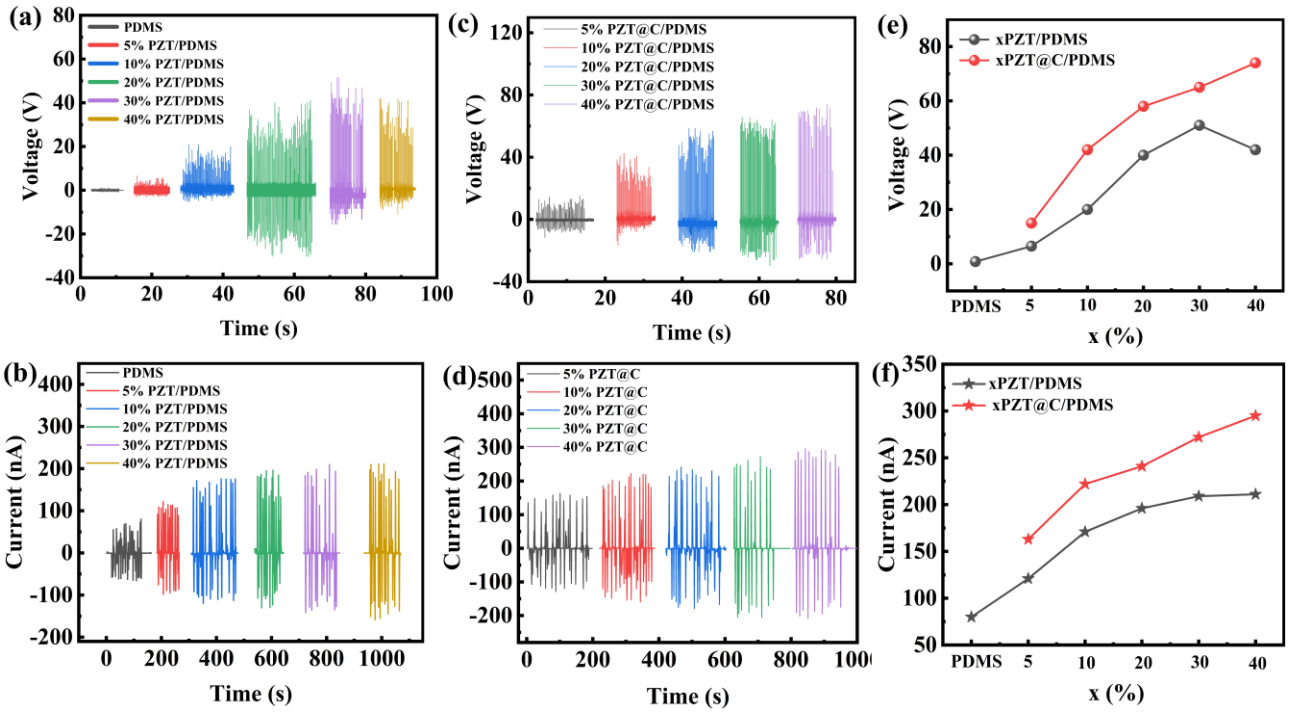


Figure 6. (**a**) Output voltages and (**b**) output currents of PZT/PDMS composite material. (**c**) Output voltages and (**d**) output currents of PZT@C/PDMS composite material. (**e**) Comparison of output voltages for composite films. (**f**) Comparison of output currents for composite films.

Figure 6c,d displays the piezoelectric signal output of the PZT@C/PDMS composite films. With the increase in PZT@C powder content, the output voltage and current of the composite film increased significantly. The output peak voltage up to ~74 V and output current up to ~295 nA are obtained in 40 wt% PZT@C/PDMS composite film, indicating outstanding electricity generation performances. Compared with PZT/PDMS film, the modified PZT@C/PDMS composite film has significantly higher electrical signal output, as shown in Figure 6e,f. The carbon shells of PZT@C particles overcome the high surface energy, van der Waals force, or electric static forces between ceramic particles, improving the dispersion uniformity of ceramic particles in the PDMS [32,33]. This results in the significant improvement of the electrical output for the composite film.

The flexible composite film can also be used as a pressure sensor. Thus, the piezoelectric signal response of 40% PZT@C/PDMS composite film to various weight impacts on film was investigated. Various weights (2 g, 5 g, 10 g, and 20 g) drop freely on the surface of the device at a height of 30 cm to simulate different degrees of impact, as demonstrated in Figure 7a. The generated voltage signals are collected in Figure 7b. With the mass of the weights increased, the generated voltage is enhanced.

The applied force on the film can be calculated according to the equation $\Delta mgh/\Delta t$, where Δmgh is the change in momentum of the ball that is fully transferred to the film, and Δt is the interaction time of the ball on the film. The interaction time (Δt) is approximately 10 ms, as displayed in the magnified voltage pulse of Figure 7c. Δmgh is quantified as mgh after the ball comes to a complete stop on the surface of the device, where m is the weight of the ball, g is the acceleration of gravity, and h is the height of descent. The detailed calculations are listed in Table S1.

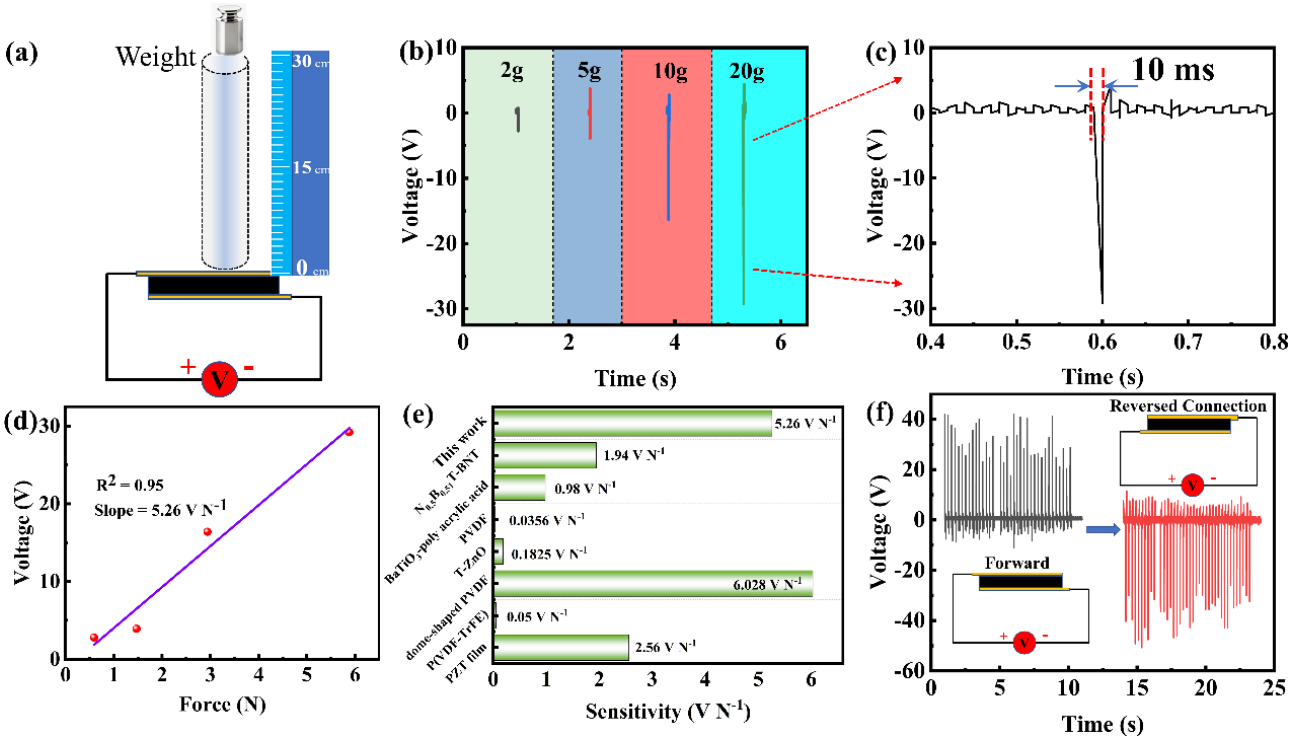


Figure 7. (**a**) Schematic diagram of a composite film excited by a freely falling weight at 30 cm. (**b**) Output voltages obtained by free-fall impact of weights of different masses on the composite film. (**c**) A magnified voltage pulse of (**b**). (**d**) Dependence of output voltage on the external force. (**e**) This work is plotted against the reported output sensitivity of some inorganic or organic films. (**f**) Output voltages of 40% PZT@C/PDMS in both forward and reversed connection for switching polarity tests.

The composite film has a sensitivity of 5.26 V N^{-1} and a linearity of 0.95, as depicted in Figure 7d. To evaluate where the level of the film sensitivity lies, the related parameters of recently reported piezoelectric organic, inorganic, or composite films are plotted in Figure 7e and Table S2 [34–40]. In comparison, the outstanding sensitivity in this work is extremely close to that of dome-shaped PVDF (6.028 V N^{-1}) and superior to other film series, such as T-ZnO (0.1825 V N^{-1}), P(VDF-TrFE) (0.05 V N^{-1}), and PZT film (2.56 V N^{-1}). Therefore, these results indicate the 40% PZT@C/PDMS film is strongly sensitive to external forces. In order to clarify the piezoelectric output, Figure 7f depicts a switching polar test, where the reversed negative and positive signals correspond to the reversed electrodes only. The results indicate that the output voltage signal is generated by the piezoelectricity of the PZT@C/PDMS film, and thus ruling out the effect of friction electricity.

Usually, the Lewis double layer [41] is introduced to comprehend the reason for improved piezoelectric characteristics for PZT@C/PDMS composite materials. The model is composed of the Stern layer and Gouy-Chapman diffusion layer. The first layer along the PZT ceramic powder interface is defined as the stern layer, which generates counter charge in the polymer materials (PDMS). The second layer, the Gouy-Chapman diffusion layer, is adjacent to the Stern layer. This layer is filled with mobile charges and plays an essential role in the piezoelectric response for ceramic-polymer composites [42].

Figure 8a presents a schematic of the carbon shell structure with a diffuse electric double layer. Based on the Lewis model, in this work, a carbon shell (interface region) is introduced between PZT ceramic powder and the polymer matrix (PDMS). Due to better electrical conductivity, the carbon shell provides a more efficient region for the accumulation of mobile charges compared to the PDMS material. In particular, the graphite-like carbon is the main component of the carbon shell structure, which is more likely to accumulate a large number of mobile charges compared with the Lewis model. This leads to the local

electric field around the PZT ceramic NPs being significantly enhanced, and it is conducive to generating sufficient polarization under an applied external electric field [43].

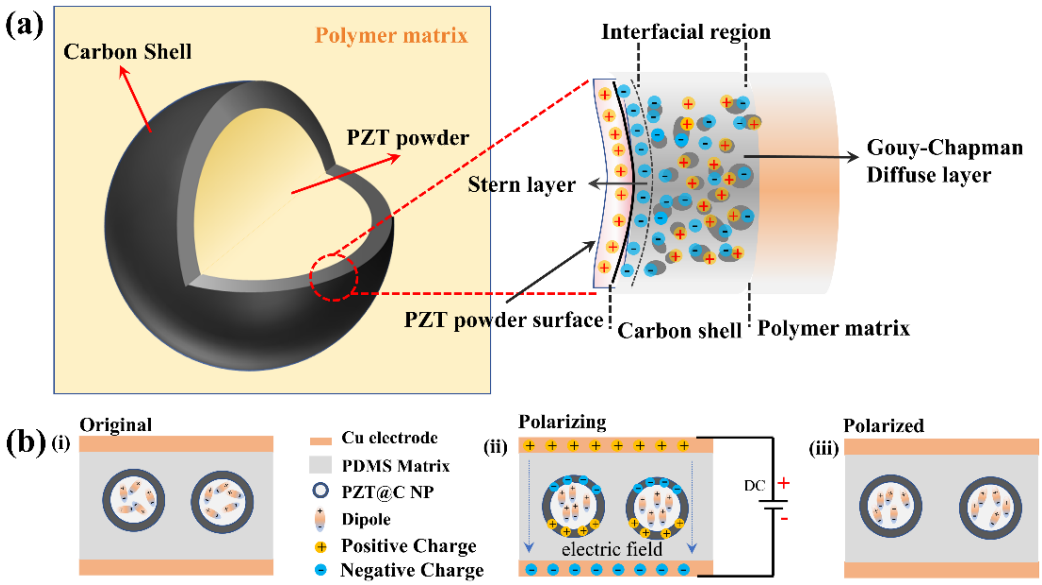


Figure 8. (**a**) Schematic of a PZT@C ceramic particle structure and the diffuse electric double layer with carbon shell structure. (**b**) Schematic illustration of the polarization principle of PZT@C/PDMS composites under high DC field.

In addition, the mechanism of polarization for the PZT@C/PDMS composite films is illustrated in Figure 8b. In this case, deformation of the structure of the composite film results in a potential difference between the positive and negative electrodes of the material. The potential difference will drive a directional flow of charge, thus generating an electrical output signal in the external circuit. Specifically, in the unpolarized state (Figure 8b(i)), the piezoelectric phase is composed of disorganized arrangements of ferroelectric dipoles, in which the macroscopic piezoelectric behavior (such as output voltage and current) cannot be observed. As shown in Figure 8b(ii), during the polarization process, mobile charges within the carbon shells are shifted and rearranged when a high DC electric field is applied. The graphite-like carbon can induce and trap mobile charges compared to PDMS materials owing to its better electroactivity, which significantly enhances the partial electric field around the PZT NPs. This enhanced localized electric field can drive the high alignment of dipoles, thus promoting the piezoelectric properties of PZT@C/PDMS composite films [30]. After polarization (Figure 8b(iii)), the polarization direction of the composite film converges with the direction of the applied external polarization voltage. The rearranged domains maintain a permanent polarization even after the poling voltage is removed. The piezoelectric effect for the polarized composite film is demonstrated in Figure S6.

3.3. The Application of Human Activity Monitoring and Pressure Monitoring

In order to prove the ability to detect human motion of composite film, the PZT@C/PDMS composite film is simply encapsulated using PI tape. Figure 9a illustrates the schematic diagram of wearable sensors to monitor the movement of different joints in the human body, including finger bending (Figure 9b), wrist flexion (Figure 9c), elbow flexion (Figure 9d,e), knee bending (Figure 9f), and foot stepping (Figure 9g). Apparently, the device outputs piezoelectric voltages up to about 18 V, 20 V, 15 V, 13 V, 21 V, and 40 V for finger bending, wrist bending, elbow bending (sensor affixed to the medial and lateral elbow joints), knee bending, and foot stepping actions, respectively. When different parts of the human body move periodically, for example, finger bending and elbow joints bending repeatedly, the total polarization of piezoelectric film changes due to the deformation of the sensors are driven by force, resulting in a potential difference. Additionally, the output voltage signal

of this pressure sensor has a strong uniform consistency without significant fluctuations. The results confirm the wearability of the piezoelectric sensor and the possibility of biomechanical sensing, which have great potential to be used as self-powered devices to monitor human movement.

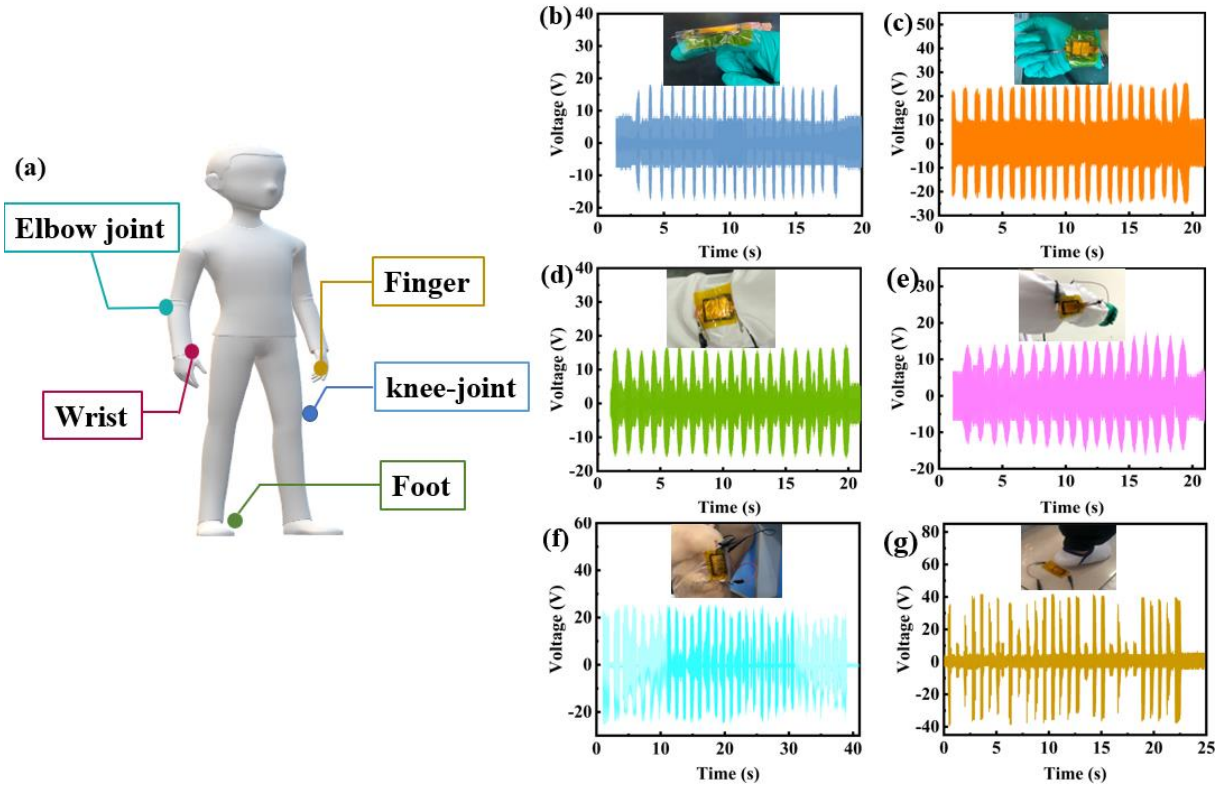


Figure 9. (**a**) The schematic diagram of wearable sensors monitoring the movement of different parts of the body. Output voltage of the device under different condition: (**b**) finger bending, (**c**) wrist flexion, (**d**) elbow flexion internal sticking, (**e**) external application of elbow joint, (**f**) knees bending, and (**g**) foot stepping.

In order to study the feasibility of applying this piezoelectric sensor to pressure monitoring, the pressure sensor is encapsulated to improve the robustness of the device, as evidenced in Figure S7. Figure S8 reveals the output voltages of the encapsulated PZT@C/PDMS pressure sensor under the condition of excitation by hand tapping. The corresponding voltages dropped to about 1/2 times the original values in Figure 6c, but this still has an obvious conversion characteristic from force to electricity. The lower magnitude of electrical output can be derived from the confinement effect of the encapsulating material, i.e., the copper foil. Figure S9 reveals the pressure sensor in the cases of surface mounting (I) and shallow burial (II), respectively. As demonstrated in Figure 10a, the oscilloscope captures an output voltage of approximately 17 V when the concrete sample surface sensor is tapped with a hammer. When the concrete sample directly above the sensor is tapped with a hammer, the output voltage (~6 V) of the pressure sensor is revealed in Figure 10b.

Compared to the surface-mounted sensors, the output voltage of the shallow-buried sensors is significantly lower by 2/3, which may stem from the list of reasons below: (i) The buried sensor is difficult to deform due to the enhanced density degree of concrete after hydration reaction. (ii) The external skeleton of the concrete absorbs the impact of the hammer blow, making the voltage output from the sensor weak. Therefore, this result suggests that a surface-attached sensor should be prioritized in practical applications.

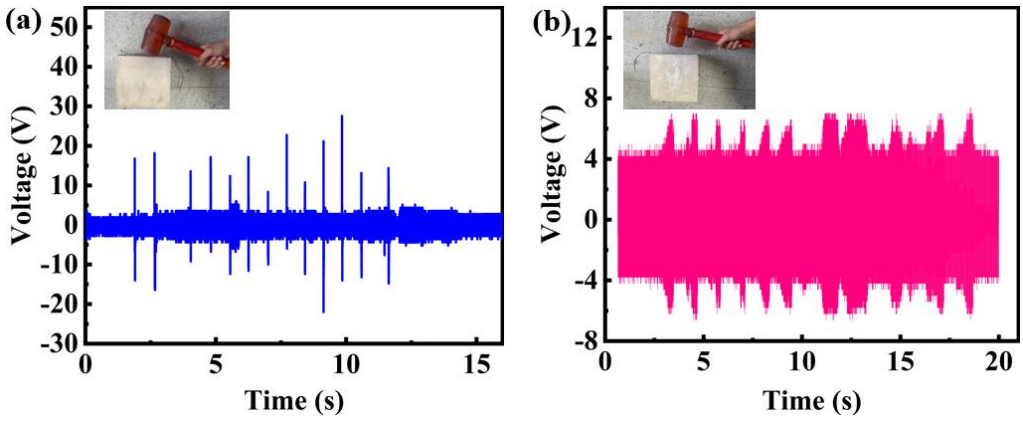


Figure 10. Output voltages of the pressure sensor: (**a**) the sensor attached to the surface of concrete, (**b**) the sensor embedded in concrete for about 1 cm.

4. Conclusions

In summary, a series of PZT@C/PDMS composite films were successfully prepared, and the carbon coating was introduced on the surface of the PZT piezoceramic NPs in order to enhance their piezoelectric properties. Compared with the PZT/PDMS composite, the PZT@C/PDMS composite film displays a significant enhancement in piezoelectric property and electrical output. The optimal output voltage, output current, and sensitiveness of the 40%PZT@C/PDMS composite reach up to ~74 V, ~295 nA, and 5.26 V N^{-1}, respectively. For the actual application, the device can be applied both in monitoring human body motions and pressure changes.

Supplementary Materials: The following supporting information can be downloaded at: https://www.mdpi.com/article/10.3390/coatings14101269/s1, Figure S1. Schematic diagram of PZT piezoceramic prepared by the conventional solid-state method. Figure S2. Piezoelectric constant d_{33} of PZT ceramic. Figure S3. TEM images of PZT@C powder with different mass ratios of PZT and PDA: (a) 2:1, (b) 4:1, (c) 6:1 and (d) 8:1. Figure S4. The Raman spectra of PZT and PZT@C ceramic powder. Figure S5. SEM images of (a) 40% PZT/PDMS and (b) 40% PZT@C/PDMS composite film cross section. Table S1. The calculated forces based on different weights, and corresponding output voltages. Table S2. Parameter comparison of different sensors. Figure S6. The schematic illustration of dipole alignment during applied pressure processes of film: (a) no impacting, (b) impacting and (c) releasing. Figure S7. Schematic diagram of PZT@CPDMS piezoelectric sensor after packaging. Figure S8. Output voltage of 40% PZT@CPDMS piezoelectric sensor after packaging. Figure S9. Optical picture of concrete specimens cured for 28 days after embedding sensor: (a) vertical view. (b) front view.

Author Contributions: Conceptualization: methodology, writing—review and editing, C.L. (Chungang Li); resources, visualization, writing—review and editing, C.L. (Chao Li); investigation, methodology, resources, formal analysis, Y.W.; data curation, resources, visualization, Y.Z.; data curation, resources, supervision, F.Y.; formal analysis, investigation, validation, visualization, G.D.; project administration, supervision, visualization, X.L.; writing—review and editing, funding acquisition, and C.Y. and S.H. All authors have read and agreed to the published version of the manuscript.

Funding: This work was supported by the Shandong provincial key research and development plan (Grant No. 2022CXPT045), the Taishan Scholars Program (Grant No. tstp20221130), and the National Natural Science Foundation of China (Grant No. 51972144).

Institutional Review Board Statement: Not applicable.

Informed Consent Statement: Not applicable.

Data Availability Statement: The data that support the findings of this study are available within the article.

Conflicts of Interest: The authors declare no conflict of interest.

References

1. Sasikumar, R.; Cho, S.; Waqar, A.; Ishfaque, A.; Choi, D.; Kim, B. Microcrack-assisted piezoelectric acoustic sensor based on f-MWCNTs/BaTiO3@PDMS nanocomposite and its self-powered voice recognition applications. *Chem. Eng. J.* **2024**, *479*, 147297. [CrossRef]
2. Zhao, J.; Li, F.; Wang, Z.; Dong, P.; Xia, G.; Wang, K. Flexible PVDF nanogenerator-driven motion sensors for human body motion energy tracking and monitoring. *J. Mater. Sci. Mater. Electron.* **2021**, *32*, 14715–14727. [CrossRef]
3. Yuan, M.; Ma, R.; Ye, Q.; Bai, X.; Li, H.; Yan, F.; Liu, C.; Ren, Y.; Wang, Z. Melt-stretched poly(vinylidene fluoride)/zinc oxide nanocomposite films with enhanced piezoelectricity by stress concentrations in piezoelectric domains for wearable electronics. *Chem. Eng. J.* **2023**, *455*, 140771. [CrossRef]
4. Yan, J.; Ma, Y.; Jia, G.; Zhao, S.; Yue, Y.; Cheng, F.; Zhang, C.; Cao, M.; Xiong, Y.; Shen, P.; et al. Bionic MXene based hybrid film design for an ultrasensitive piezoresistive pressure sensor. *Chem. Eng. J.* **2022**, *431*, 133458. [CrossRef]
5. Yu, C.; Liu, K.; Xu, J.; Ye, M.; Yang, T.; Qi, T.; Zhang, Y.; Xu, H.; Zhang, H. High-performance multifunctional piezoresistive/piezoelectric pressure sensor with thermochromic function for wearable monitoring. *Chem. Eng. J.* **2023**, *459*, 141648. [CrossRef]
6. Zhang, D.; Yin, R.; Zheng, Y.; Li, Q.; Liu, H.; Liu, C.; Shen, C. Multifunctional MXene/CNTs based flexible electronic textile with excellent strain sensing, electromagnetic interference shielding and Joule heating performances. *Chem. Eng. J.* **2022**, *438*, 135587. [CrossRef]
7. Su, Y.; Li, Q.; Amagat, J.; Chen, M. 3D spring-based piezoelectric energy generator. *Nano Energy* **2021**, *90*, 106578. [CrossRef]
8. Yuan, X.; Gao, X.; Shen, X.; Yang, J.; Li, Z.; Zhao, S. A 3D-printed, alternatively tilt-polarized PVDF-TrFE polymer with enhanced piezoelectric effect for self-powered sensor application. *Nano Energy* **2021**, *85*, 105985. [CrossRef]
9. Kim, Y.-G.; Song, J.-H.; Hong, S.; Ahn, S.-H. Piezoelectric strain sensor with high sensitivity and high stretchability based on kirigami design cutting. *NPJ Flex. Electron.* **2022**, *6*, 52. [CrossRef]
10. Zhao, L.; Yu, S.; Li, J.; Song, Z.; Wang, X. Highly Reliable Sensitive Capacitive Tactile Sensor with Spontaneous Micron-Pyramid Structures for Electronic Skins. *Macromol. Mater. Eng.* **2022**, *307*, 2200192. [CrossRef]
11. Li, Z.; Zhao, K.; Wang, J.; Wang, B.; Lu, J.; Jia, B.; Ji, T.; Han, X.; Luo, G.; Yu, Y.; et al. Sensitive, Robust, Wide-Range, and High-Consistency Capacitive Tactile Sensors with Ordered Porous Dielectric Microstructures. *ACS Appl. Mater. Interfaces* **2024**, *16*, 7384–7398. [CrossRef] [PubMed]
12. Ma, Z.; Lu, S.; Wu, Y.; Zhang, X.; Wei, Y.; Mawignon, F.J.; Qin, L.; Shan, L. Pressure-Activatable Liquid Metal Composites Flexible Sensor with Antifouling and Drag Reduction Functional Surface. *ACS Appl. Mater. Interfaces* **2023**, *15*, 54952–54965. [CrossRef] [PubMed]
13. Lu, H.; Chen, B.; Lai, X.; Li, H.; Zeng, X. Porous reduced graphene oxide@multi-walled carbon nanotubes/polydimethylsiloxane piezoresistive pressure sensor for human motion detection. *Mater. Today Nano* **2024**, *28*, 100512. [CrossRef]
14. Nguyen, T.; Dinh, T.; Phan, H.-P.; Pham, T.A.; Dau, V.T.; Nguyen, N.-T.; Dao, D.V. Advances in ultrasensitive piezoresistive sensors: From conventional to flexible and stretchable applications. *Mater. Horiz.* **2021**, *8*, 2123–2150. [CrossRef] [PubMed]
15. Pyo, S.; Lee, J.; Bae, K.; Sim, S.; Kim, J. Recent Progress in Flexible Tactile Sensors for Human-Interactive Systems: From Sensors to Advanced Applications. *Adv. Mater.* **2021**, *33*, e2005902. [CrossRef] [PubMed]
16. Pongampai, S.; Charoonsuk, T.; Pinpru, N.; Pulphol, P.; Vittayakorn, W.; Pakawanit, P.; Vittayakorn, N. Triboelectric-piezoelectric hybrid nanogenerator based on BaTiO3-Nanorods/Chitosan enhanced output performance with self-charge-pumping system. *Compos. Part B Eng.* **2021**, *208*, 108602. [CrossRef]
17. Zhang, G.; Zhao, P.; Zhang, X.; Han, K.; Zhao, T.; Zhang, Y.; Jeong, C.K.; Jiang, S.; Zhang, S.; Wang, Q. Flexible three-dimensional interconnected piezoelectric ceramic foam based composites for highly efficient concurrent mechanical and thermal energy harvesting. *Energy Environ. Sci.* **2018**, *11*, 2046–2056. [CrossRef]
18. Xu, X.; Wang, X.; Jiang, H.; Wang, M.; Ma, W.; Liu, W.; Wang, S.; Ma, S. High-performance ethanol sensor based on self-assembled $BaTiO_3$/ZnO composite hierarchical nanostructure. *Sens. Actuators A* **2024**, *372*, 115387. [CrossRef]
19. Kang, H.B.; Han, C.S.; Pyun, J.C.; Ryu, W.H.; Kang, C.-Y.; Cho, Y.S. (Na,K)NbO_3 nanoparticle-embedded piezoelectric nanofiber composites for flexible nanogenerators. *Compos. Sci. Technol.* **2015**, *111*, 1–8. [CrossRef]
20. Jian, G.; Jiao, Y.; Meng, Q.; Guo, Y.; Wang, F.; Zhang, J.; Wang, C.; Moon, K.-S.; Wong, C.-P. Excellent high-temperature piezoelectric energy harvesting properties in flexible polyimide/3D $PbTiO_3$ flower composites. *Nano Energy* **2021**, *82*, 105778. [CrossRef]
21. Tao, K.; Yi, H.; Tang, L.; Wu, J.; Wang, P.; Wang, N.; Hu, L.; Fu, Y.; Miao, J.; Chang, H. Piezoelectric ZnO thin films for 2DOF MEMS vibrational energy harvesting. *Surf. Coat. Technol.* **2019**, *359*, 289–295. [CrossRef]
22. Zhu, Q.; Song, X.; Chen, X.; Li, D.; Tang, X.; Chen, J.; Yuan, Q. A high performance nanocellulose-PVDF based piezoelectric nanogenerator based on the highly active CNF@ZnO via electrospinning technology. *Nano Energy* **2024**, *127*, 109741. [CrossRef]
23. Li, H.; Wu, B.; Lin, C.; Wu, X.; Lin, T.; Gao, M.; Tao, H.; Wu, W.; Zhao, C. Microscopic origin and relevant grain size effect of discontinuous grain growth in $BaTiO_3$-based ferroelectric ceramics. *J. Mater. Sci. Technol.* **2023**, *164*, 119–128. [CrossRef]
24. Islam, M.J.; Lee, H.; Lee, K.; Cho, C.; Kim, B. Piezoelectric Nanogenerators Fabricated Using Spin Coating of Poly(vinylidene fluoride) and ZnO Composite. *Nanomaterials* **2023**, *13*, 1289. [CrossRef] [PubMed]
25. Ham, S.S.; Lee, G.-J.; Hyeon, D.Y.; Kim, Y.-g.; Lim, Y.-w.; Lee, M.-K.; Park, J.-J.; Hwang, G.-T.; Yi, S.; Jeong, C.K.; et al. Kinetic motion sensors based on flexible and lead-free hybrid piezoelectric composite energy harvesters with nanowires-embedded electrodes for detecting articular movements. *Compos. Part B Eng.* **2021**, *212*, 108705. [CrossRef]

26. Kumar, M.; Kulkarni, N.D.; Kumari, P. Piezoelectric performance enhancement of electrospun functionally graded PVDF/BaTiO3 based flexible nanogenerators. *Mater. Res. Bull.* **2024**, *174*, 112739. [CrossRef]
27. Xia, X.; Jiang, X.; Zeng, J.; Zheng, L.; Man, Z.; Zeng, H.; Li, G. Critical state to achieve a giant electric field-induced strain with a low hysteresis in relaxor piezoelectric ceramics. *J. Mater.* **2021**, *7*, 1143–1152. [CrossRef]
28. He, D.; Zhao, Y.; Li, W.; Shang, L.; Wang, L.; Zhang, G. Superior mechanical and tribological properties governed by optimized modulation ratio in WC/a-C nano-multilayers. *Ceram. Int.* **2021**, *47*, 16861–16869. [CrossRef]
29. Peng, J.; Chen, N.; He, R.; Wang, Z.; Dai, S.; Jin, X.J.A.C. Electrochemically Driven Transformation of Amorphous Carbons to Crystalline Graphite Nanoflakes: A Facile and Mild Graphitization Method. *Angew. Chem.* **2017**, *56*, 1751–1755. [CrossRef]
30. Zhou, Z.; Du, X.; Zhang, Z.; Luo, J.; Niu, S.; Shen, D.; Wang, Y.; Yang, H.; Zhang, Q.; Dong, S. Interface modulated 0-D piezoceramic nanoparticles/PDMS based piezoelectric composites for highly efficient energy harvesting application. *Nano Energy* **2021**, *82*, 105709. [CrossRef]
31. Shen, Z.-H.; Tang, T.-X.; Wang, J.; Zhou, M.-J.; Liu, H.-X.; Chen, L.-Q.; Shen, Y.; Nan, C.-W. Computation-guided design of flexible piezoelectric composites by optimizing charge-stress transmission. *Nano Energy* **2023**, *117*, 108933. [CrossRef]
32. Luo, H.; Zhou, X.; Ellingford, C.; Zhang, Y.; Chen, S.; Zhou, K.; Zhang, D.; Bowen, C.R.; Wan, C. Interface design for high energy density polymer nanocomposites. *Chem. Soc. Rev.* **2019**, *48*, 4424–4465. [CrossRef] [PubMed]
33. Dang, Z.M.; Yuan, J.K.; Yao, S.H.; Liao, R.J. Flexible Nanodielectric Materials with High Permittivity for Power Energy Storage. *Adv. Mater.* **2013**, *25*, 6334–6365. [CrossRef] [PubMed]
34. Zhao, K.; Shan, Z.; Li, D.; Ma, R.; Li, P.; Wang, F.; Cui, Y.; Zhong, Z.; Zhang, K. PZT thick film element balancing flexibility with piezoelectricity fabricated by electrohydrodynamics jet printing used for micro power generator. *Ceram. Int.* **2024**, *50*, 26908–26917. [CrossRef]
35. Kim, M.-S.; Ahn, H.-R.; Lee, S.; Kim, C.; Kim, Y.-J. A dome-shaped piezoelectric tactile sensor arrays fabricated by an air inflation technique. *Sens. Actuators A* **2014**, *212*, 151–158. [CrossRef]
36. Wang, K.; Ma, J.-N.; Zhang, C.-Y.; Pei, Z.; Tang, W.-T.; Zhang, Q. Self-powered high-sensitivity piezoelectric sensors for end-fixture force sensing in surgical robots based on T-ZnO. *Colloids Surf. A* **2024**, *697*, 134424. [CrossRef]
37. Yin, H.; Guan, Y.; Li, Y.; Zheng, Z.; Guo, Y. Modulation of piezoelectricity and mechanical strength in piezoelectric composites based on $N_{0.5}B_{0.51}$T-BNT nanocubes towards human-machine interfaces. *Nano Energy* **2023**, *118*, 109044.
38. Khan, S.; Tinku, S.; Lorenzelli, L.; Dahiya, R.S. Flexible Tactile Sensors Using Screen-Printed P(VDF-TrFE) and MWCNT/PDMS Composites. *IEEE Sens. J.* **2015**, *15*, 3146–3155. [CrossRef]
39. Huang, X.; Ma, Z.; Xia, W.; Hao, L.; Wu, Y.; Lu, S.; Luo, Y.; Qin, L.; Dong, G. A high-sensitivity flexible piezoelectric tactile sensor utilizing an innovative rigid-in-soft structure. *Nano Energy* **2024**, *129*, 110019. [CrossRef]
40. Zhao, B.; Su, Y.; Xue, R.; Wang, Y.; Miao, L.; Yao, M.; Yu, H.; Zhao, W.; Hu, D.J.M.C.F. Degradable flexible piezoelectric nanogenerator based on two-dimensional barium titanate nanosheets and polylactic acid. *Mater. Chem. Front.* **2023**, *7*, 3082–3092. [CrossRef]
41. Lewis, T. Interfaces are the dominant feature of dielectrics at the nanometric level. *IEEE Trans. Dielectr. Electr. Insul.* **2004**, *11*, 739–753. [CrossRef]
42. Prateek; Thakur, V.K.; Gupta, R.K. Recent Progress on Ferroelectric Polymer-Based Nanocomposites for High Energy Density Capacitors: Synthesis, Dielectric Properties, and Future Aspects. *Chem. Rev.* **2016**, *116*, 4260–4317. [CrossRef] [PubMed]
43. Chen, Q.; Shen, Y.; Zhang, S.; Zhang, Q.M. Polymer-Based Dielectrics with High Energy Storage Density. *Annu. Rev. Mater. Res.* **2015**, *45*, 433–458. [CrossRef]

Disclaimer/Publisher's Note: The statements, opinions and data contained in all publications are solely those of the individual author(s) and contributor(s) and not of MDPI and/or the editor(s). MDPI and/or the editor(s) disclaim responsibility for any injury to people or property resulting from any ideas, methods, instructions or products referred to in the content.